Inorganic Chemistry
Article
pubs.acs.org/IC

Synthesis of Novel Two-Phase Co@SiO$_2$ Nanorattles with High Catalytic Activity

Nan Yan, Ziang Zhao, Yan Li, Fang Wang, Hao Zhong, and Qianwang Chen*

Hefei National Laboratory for Physical Sciences at Microscale and Department of Materials Science & Engineering & Collaborative Innovation Center of Suzhou Nano Science and Technology, University of Science and Technology of China, Hefei 230026, People's Republic of China

S *Supporting Information*

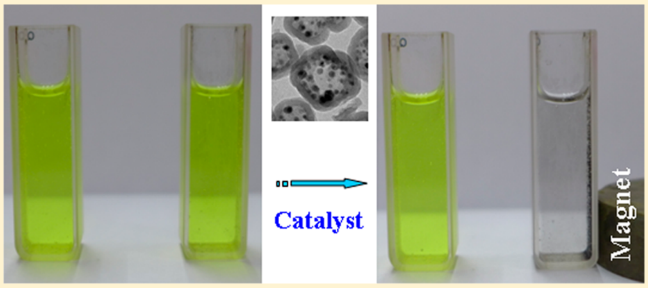

ABSTRACT: Noble metal nanocatalysts with remarkable catalytic properties have attracted much attention; however, the high cost of these materials limits their industrial applications. Here, we design and prepare Co@SiO$_2$ nanorattles as a mixture of hcp-Co and fcc-Co phases as a substitute. The nanorattles exhibit both superior catalytic activity and high stability for the reduction of *p*-nitrophenol. The reduction rate nearly follows pseudo-first-order kinetics, and the reaction rate constant is as high as 0.815 min^{-1} and is maintained at 0.565 min^{-1} even after storing for one month, which is higher than that reported for noble metal nanocatalysts. Such an excellent property can be attributed to the novel two-phase composition and rattle-type structure.

1. INTRODUCTION

During the past decade, metal nanoparticles have attracted considerable attention due to their unique physicochemical properties and potential applications.[1] One of the most promising applications of metal nanoparticles is in heterogeneous catalysis.[2] Noble metal nanocatalysts have received great interest primarily due to their stable properties and superior catalytic performances.[3] However, owing to the high cost of noble metals, alternative catalysts based on nonprecious metals have been actively investigated. As an important magnetic metal material, cobalt nanoparticles have extensive applications in high-density magnetic recording, sensors, and heterogeneous catalysis.[4] The catalytic performance of cobalt has been investigated in several fields. For example, cobalt has been used in the industry for hydrocarbon synthesis in the Fischer–Tropsch reaction.[5a] Qi et al. have prepared flower-like cobalt nanostructures and studied their catalytic activity in the Heck reaction.[5b] The application of cobalt-based catalysts in other catalytic reactions such as methanol oxidation and reduction of nitric oxide has also been reported.[6] Currently, the recovery and reuse of catalysts in catalytic reactions has attracted growing interest to meet the requirements for environmentally friendly and cost-effective reaction processes. This is because nanocatalysts in heterogeneous catalysis are difficult to isolate or separate from the reaction system due to their small size and well-dispersed nature.[7] Several methodologies have been attempted to solve this problem. Among them, the recovery of nanocatalysts from the product mixture using an external magnet has been emerging recently as a new and effective technique.[8] Therefore, a quick response to magnetic fields is desirable for nanocatalysts. In this regard, ferromagnetic cobalt nanoparticles meet the demand. However, cobalt nanocatalysts are less active than noble metals such as Pd, Pt, and Au. Furthermore, cobalt nanoparticles have the tendency to aggregate in order to reduce their surface energy.[9,10] Some improvements have been achieved. For instance, cobalt nanoparticles were deposited on porous silica or carbon,[11] but their catalytic activities are still lower than noble metal nanocatalysts. It is therefore crucial to design and prepare novel structures of cobalt nanocatalysts to realize high catalytic activity and long-period stability.

One method for enhancing the catalytic performance is to prepare nanoparticles with mixed-phase junction structures. Several previous reports have confirmed that the proper junctions formed in semiconductor-based photocatalysts could lead to enhanced activity in either hydrogen or oxygen half-reactions.[12] The enhanced photocatalytic performance results from efficient charge separation and transfer across the phase junction.[12a] On the basis of these results, it is suggested that making phase junctions in metal cobalts may also change the surface charge distribution owing to the changed density of states in different crystal phases of cobalt,[13] thus improving the catalytic performance. Furthermore, rattle-type nanoparticles (nanorattles) have an interesting structure comprising a thin shell with monodisperse nanoparticle cores encapsulated. The heterostructure with different types of shell and core makes the nanorattles multifunctional nanomaterials.[14] One of their most important applications is as nanocatalysts. The hollow shell can prevent the cores with catalytic activity from gathering together

Received: May 11, 2014
Published: August 20, 2014

© 2014 American Chemical Society

and allow the fast diffusion of reactants and products through the shell. Simultaneously, the movable cores as catalysts can also enhance the catalytic activity. For example, Song's group reported a kind of nanorattle composed of mesoporous silica hollow spheres and Pd nanoparticles residing inside the spheres. The nanorattles exhibited high catalytic activity in Suzuki coupling reactions with 99.5% yield in 3 min.[15] Recently, various synthesis methods have been developed to obtain nanorattles, including selective etching, a template-assisted process, and Kirkendall effects.[16] Our group has reported a novel route called "*in situ* thermal decomposition with self-templating" to prepare Co_3O_4@SiO_2 nanorattles with a clean crystal surface, which exhibited excellent catalytic activity for CO oxidation.[17,18]

Herein, we developed a method to prepare Co@SiO_2 nanorattles by annealing $Co_3[Co(CN)_6]_2$@SiO_2 core−shell nanoparticles in N_2 at different temperatures. At an appropriate temperature, the hcp and fcc phase junctions of cobalt can be generated within the SiO_2 shells. The catalytic activity of Co@SiO_2 nanorattles toward reduction of 4-nitrophenol to 4-aminophenol by $NaBH_4$ has also been evaluated.

2. EXPERIMENTAL SECTION

2.1. Synthesis. All chemicals are of analytical grade and used without purification. The following steps were conducted in our synthetic experiments: The $Co_3[Co(CN)_6]_2$ nanoparticles were synthesized following the previous reports of our group.[18] A 60 mg amount of as-prepared $Co_3[Co(CN)_6]_2$ nanoparticles and 0.35 mL of tetraethyl orthosilicate (TEOS) were dispersed in 30 mL of ethanol. After being intensely sonicated for 10 min, 6 mL of a concentrated ammonia solution (28 wt %) was added dropwise in 5 min. The reaction was allowed to proceed at 45 °C for 4 h under continuous mechanical stirring. The resulting $Co_3[Co(CN)_6]_2$@SiO_2 core/shell nanoparticles were centrifuged and washed twice with distilled water, then air-dried at 60 °C. The annealing process in N_2 was performed at 600 °C for 1 h with a heating rate of 10 °C min^{-1} to obtain Co@SiO_2 nanorattles. The weight ratio of Co is 13.2% according to ICP characterization.

2.2. Characterization. The powder X-ray diffraction (XRD) patterns were collected on a Japan Rigaku D/MAX-cA X-ray diffractometer equipped with Cu Ka radiation over the 2θ range of 10−80°. Thermogravimetric analysis (TGA)-IR-MS was carried out using a Pyris 1 thermogravimetric analyzer combined with a Frontier and Clarus 5Q 8 T (PerkinElmer) under a nitrogen gas flow at a heating rate of 20 °C min^{-1} in a temperature range from 25 to 850 °C. Scanning electron microscopy (SEM) images were obtained on a JEOL JSM-6700 M scanning electron microscope. Transmission electron microscopy (TEM) images were obtained on a Hitachi H-800 transmission electron microscope, using an accelerating voltage of 200 kV. High-resolution transmission electron microscopy (HRTEM) images were taken on a JEOL-2010 transmission electron microscope, which was operated at 200 kV. The energy-dispersive X-ray spectroscopy (EDS) mapping was characterized using a scanning transmission electron microscope (STEM, JEM 2100F). Specific surface areas were calculated from the results of N_2 physisorption at 77 K (Micromeritics ASAP 2020) by using the BET (Brunauer−Emmet−Teller) and BJH (Barrett−Joyner−Halenda) analyses. The magnetic property of the product was evaluated by a superconducting quantum interference device (SQUID) magnetometer (Quantum Design MPMS XL-7) at room temperature. The FT-IR spectrum was obtained using a Magna-IR 750 spectrometer in the range 500−4000 cm^{-1} with a resolution of 4 cm^{-1}. The sample was dissolved in hydrochloric acid (5 mol L^{-1}) and reacted in a Teflon-lined stainless steel autoclave at 150 °C for 8 h. The concentration of cobalt ions was measured using inductively coupled plasma (ICP)-atomic emission spectroscopy (Atomscan Advantage). X-ray photoelectron spectroscopy (XPS) was performed on an ESCALAB 250 X-ray photoelectron spectrometer with Al Kα radiation.

2.3. Catalytic Performance Measurements. The catalytic properties of Co@SiO_2 nanorattles were investigated via the reduction of *p*-nitrophenol to *p*-aminophenol by $NaBH_4$ at room temperature as a probe reaction. First, 0.1 mL of *p*-nitrophenol (0.03 M) was added to a 1 mL of $NaBH_4$ aqueous solution (0.3 M). After that, 3.9 mL of H_2O was added into the mixture. Then the mixture solution was transferred to a quartz cuvette, and 1 mg of Co@SiO_2 nanorattles was added to the above solution. The reaction progress was monitored by measuring the UV−vis absorption spectra (TU-1810) of the reaction solutions. After the reaction, the reaction mixture was extracted with ethyl acetate and was analyzed by GC-MS using an Agilent 7890A/5975C. To determine the catalytic recycling properties and the stability in air, the nanocatalysts were separated by a magnet after the first reaction, then washed thoroughly with water and ethanol, followed by drying at 60 °C for 12 h in a vacuum oven. Next, the catalysts were stored in an open centrifuge tube. A month later, the catalyst was redispersed in a new reaction system for subsequent catalytic experiments under the same reaction conditions.

3. RESULTS AND DISCUSSION

Figure 1 schematically illustrates the procedure for generating Co@SiO_2 nanorattles and the catalytic application of nanorattles for the reduction of *p*-nitrophenol. First, SiO_2 was coated on uniform $Co_3[Co(CN)_6]_2$ nanoparticles during the sol−gel process of tetraethyl orthosilicate, producing $Co_3[Co(CN)_6]_2$@SiO_2 core−shell nanoparticles. The next step was the calcination of the core−shell nanoparticles in N_2. Unlike the thermal conversion to Co_3O_4 in air, the $Co_3[Co(CN)_6]_2$ decomposed to elementary Co when annealed in N_2. The monodisperse Co nanoparticles were generated due to the Ostwald ripening effect during the process of thermal decomposition, while the porous silica shell can maintain the previous shape due to its thermal stability. In this way, Co@SiO_2 nanorattles were obtained. When used as nanocatalysts, Co@SiO_2 nanorattles could be considered as nanoreactors. *p*-Nitrophenol and $NaBH_4$ diffused into the inside of the nanorattle and adsorbed on the surface of the Co nanoparticles. Then, the reduction reaction and desorption of reaction products from the catalyst surface occurred. After the reaction, the Co@SiO_2 nanorattles could be separated by a magnet and reused in the next catalysis process.

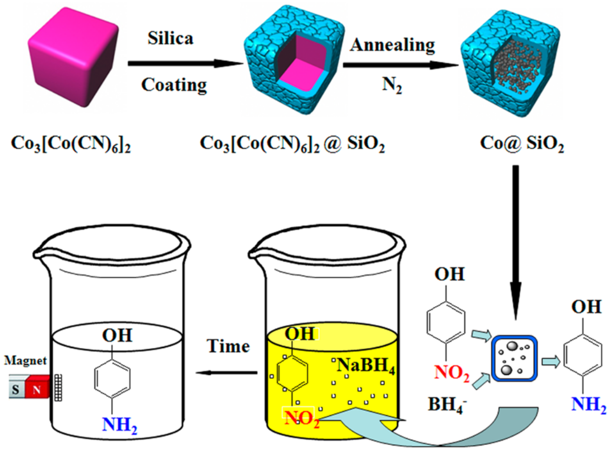

Figure 1. Schematic illustration of the formation process of a Co@SiO_2 nanorattle and the catalytic application of nanorattles in reduction of *p*-nitrophenol by $NaBH_4$.

$Co_3[Co(CN)_6]_2$ nanoparticles were prepared via a room-temperature precipitation method as reported previously.[18] From the SEM image (Figure S1), the $Co_3[Co(CN)_6]_2$ nanoparticles have been prepared in a uniform cube shape and show excellent dispersibility. After being coated with silica (shown in Figure S2), $Co_3[Co(CN)_6]_2@SiO_2$ core−shell nanoparticles can keep the cube shape and the excellent dispersibility in aqueous solutions. It is found that the surfaces become rough, which indicates the successful coating. TEM observations reveal that the solid structure of $Co_3[Co(CN)_6]_2$ nanoparticles (Figure S3) turns to a core−shell structure (Figure S4) after coating. TGA-IR-MS characterization was carried out to monitor the decomposition behavior of the precursors. The TGA curve in N_2 shown in Figure S5a reveals two decomposition steps. The first step occurred at the temperature of 50 °C, while the plateau of the curve reappeared at about 110 °C. The second step showed the change near the temperature of 540 °C. The time-dependent IR (wavenumber: 2113 and 2187 cm^{-1}, shown in Figure S5b) and MS (m/z: 52, shown in Figure S5d) revealed that the $(CN)_2$ molecules appeared after 15 min from the start, which corresponded to the temperature of 325 °C. This could be taken as the decomposition temperature of $Co_3[Co(CN)_6]_2$. After 25 min (540 °C), the $(CN)_2$ molecules disappeared, illustrating the complete decomposition of $Co_3[Co(CN)_6]_2$. According to the time-dependent IR absorbance variation of H_2O (wavenumber: 1520 and 1701 cm^{-1}, shown in Figure S5c) and time-dependent MS intensity variation of H_2O (m/z: 18, shown in Figure S5e), it is suggested that the evaporation of adsorbed water has occurred in the whole annealing process, which caused the sustained weight loss after the decomposition of $Co_3[Co(CN)_6]_2$. From the TG-DTA-MS measurements, $Co_3[Co(CN)_6]_2$ nanoparticles were decomposed at 325 °C to generate a simple cobalt substance and $(CN)_2$ gas.

$Co_3[Co(CN)_6]_2@SiO_2$ core−shell nanoparticles were annealed at 600 °C for 1 h, generating $Co@SiO_2$ nanorattles. The X-ray diffraction pattern is shown in Figure 2a. It is well known that metallic cobalt can crystallize in three different crystal structures: hexagonal closed-packed phase (hcp), face-centered cubic phase (fcc), and primitive cubic phase.[19] Generally, the fcc structure is thermodynamically preferred above 450 °C and the hcp phase is favored at lower temperatures.[20] Most previous papers reported the preparation of hcp-phase cobalt by solvothermal synthesis.[21] The XRD pattern shows a composite structure of Co nanoparticles is formed. The diffraction peaks at 41.5°, 44.2°, 47.4°, 62.3°, and 75.9° correspond to the (100), (002), (101), (102), and (110) crystal planes of the hcp-phase cobalt (JCPDS: 89-4308), while the diffraction peaks at 44.2° and 75.9° correspond to the (111) and (200) crystal planes of the fcc-phase cobalt (JCPDS: 89-4307). A weak peak at 51.5° corresponds to the (200) crystal plane of the fcc-phase cobalt. In addition, there is a weak broad band between 20° and 25°, which indicates the presence of amorphous silica. This result reveals the two-phase composition of Co nanoparticles in $Co@SiO_2$ nanorattles. The fcc and hcp phases of cobalt are close-packed structures that differ only in the stacking sequence of atomic planes in the (111) direction. A low activation energy often leads to the formation of both phases in the same sample under high-temperature crystallization techniques.[20] When annealing at 450 °C, only the hcp Co phase was found (Figure S6), while the fcc-phase Co can be obtained at 900 °C (Figure S7).

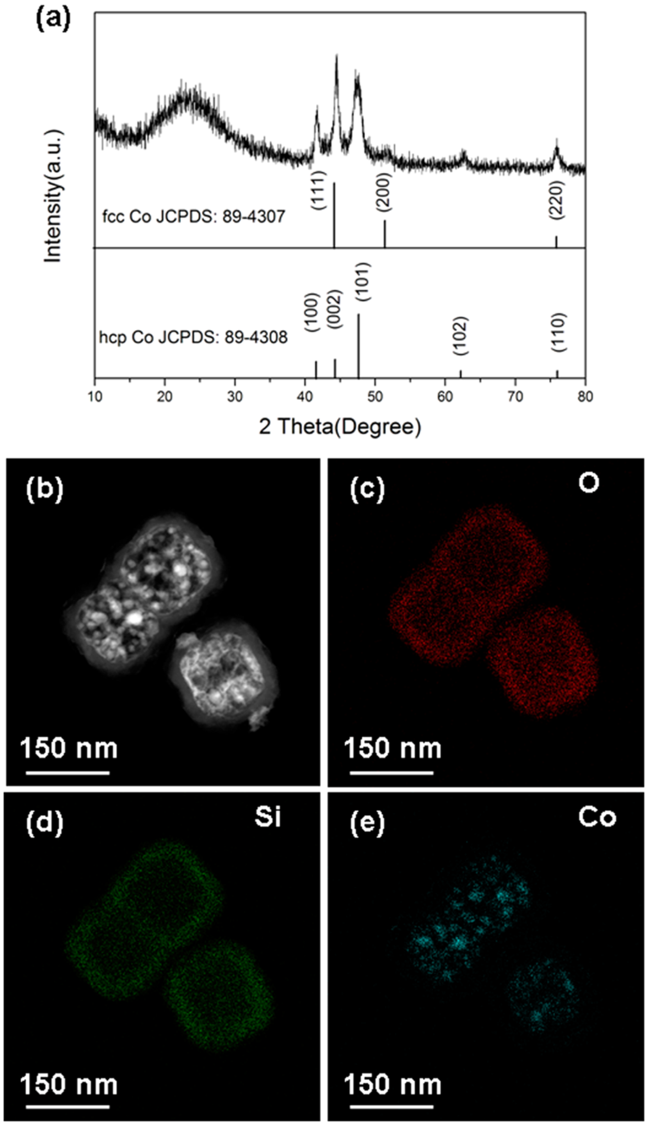

Figure 2. (a) XRD pattern of $Co@SiO_2$ nanorattles, (b) dark-field STEM image of $Co@SiO_2$ nanorattles, and (c−e) EDS mapping of the same nanoparticles, indicating the spatial distribution of O (c), Si (d), and Co (e), respectively.

Dark-field STEM (Figure 2b) and EDS mappings of the same particles (Figure 2c−e) clearly show the spatial distributions of O, Si, and Co. The EDS mappings of O and Si suggest the SiO_2 shells of nanorattles. Small Co nanoparticles exist in the inner space of SiO_2 shells, showing excellent dispersibility.

The morphology of $Co@SiO_2$ nanorattles is observed by SEM, as shown in Figure 3a,b. Figure 3a shows that the SiO_2 shells maintain the uniform cube shape with an average diameter of 130 nm after annealing. The magnified SEM image shown in Figure 3b illustrates the surface morphology of SiO_2 shells. A large amount of crevices on the surface can be observed, which has also been discussed in the formation of hollow porous silica nanocubes.[22] From the high-resolution SEM image of broken nanoparticles, it can be seen that crevices exist throughout the whole shell (Figure S8). When the nanorattles are used as nanocatalysts, these crevices are effective for reacting molecules in solution diffusing into the interior of the nanorattles. The $Co@SiO_2$ nanorattles generated at 450 °C

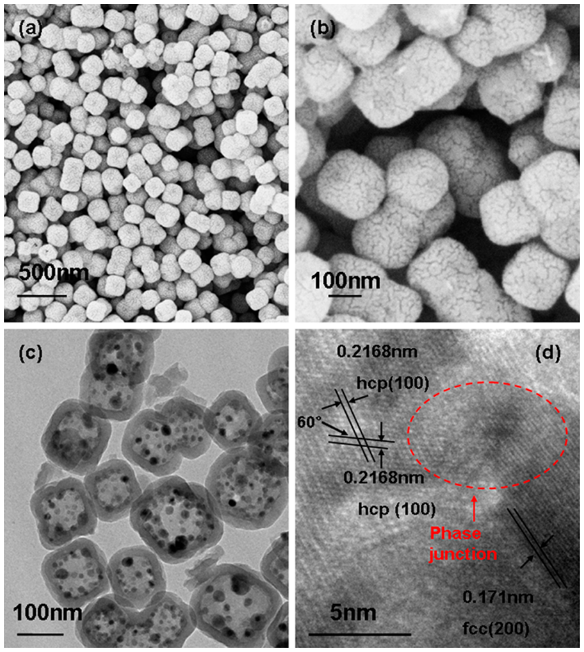

Figure 3. (a, b) SEM and (c) TEM images of Co@SiO_2 nanorattles and (d) HRTEM image of Co nanoparticles in the interior of a nanorattle.

(Figure S9) and 900 °C (Figure S10) show almost the same shape.

Figure 3c reveals the inner structure of Co@SiO_2 nanorattles. Co nanoparticles with an average particle size of 20 nm wrapped in a hollow SiO_2 shell can be clearly seen, demonstrating a typical rattle-type structure. A high-resolution TEM image of Co nanoparticles in a nanorattle is shown in Figure 3d, clearly displaying a variety of lattice fringes, which are consistent with different phases of cobalt. The lattice fringes with a spacing of 0.2168 nm (on the left side of the image) correspond to the (100) lattice plane of hcp-phase cobalt, while the lattice fringes with a spacing of 0.171 nm (on the right side of the image) correspond to the (200) plane of fcc-phase cobalt. As shown in the dashed box, such a structure can be considered as a phase junction, which may exhibit unique chemical and physical properties different from those of single-phase cobalt.[12] Figures S11 and S12 also show the rattle structure of the sample annealed at 450 and 900 °C.

The N_2 absorption−desorption isotherms at 77 K are shown in Figure S13, characteristic of a type IV with type H3 hysteresis loop, confirming the porous structure of Co@SiO_2 nanorattles. The specific surface area calculated with the BET model is 20.2 m^2 g^{-1}. Furthermore, the pore size distribution has a broad peak at 14.5 nm (Figure S14), which corresponds well with the irregular distribution of crevices on the surface of Co@SiO_2 nanorattles. The magnetic hysteresis loop (Figure S15) for Co@SiO_2 nanorattles was measured at room temperature (300 K) in an applied magnetic field of 20 000 Oe. The magnetization saturation is 24.4 emu g^{-1}, which indicates Co@SiO_2 nanorattles can be separated and recovered from the solution by a magnet. Moreover, the magnetic hysteresis loops of Co@SiO_2 nanorattles display a wasp-waist shape, which demonstrates the existence of two phases with different magnetism.[23]

The catalytic reduction of *p*-nitrophenol (Nip) to *p*-aminophenol is the most often used probe reaction to test the catalytic activity of metal nanoparticles in aqueous solution.[24] *p*-Aminophenol is also an industrial chemical intermediate in producing many analgesic and antipyretic drugs, anticorrosion lubricants, and hair-drying agents.[25] Thus, it is highly desirable to develop more efficient, durable, and eco-friendly catalytic systems to produce *p*-aminophenol. On the basis of the unique rattle-type structure, porous shell, and two-phase composition, the as-obtained Co@SiO_2 nanorattles have been investigated as heterogeneous catalysts toward the reduction of Nip. Figure 4a shows a typical catalysis process with Co@SiO_2 nanorattles. First, two quartz cuvettes were filled with 5 mL of a yellow-green aqueous solution of 0.003 mmol of Nip and 0.3 mmol of $NaBH_4$. Then 1 mg of Co@SiO_2 nanorattles was added into the right quartz cuvette. After 5 min, the color changed from yellow-green to colorless, and Co@SiO_2 nanorattles were separated by an external magnet. As a comparison, the left quartz cuvette without catalyst had no color change. Figure 4b shows the successive UV−vis spectra changes in Nip catalyzed by Co@SiO_2 nanorattles. It can be seen that the characteristic peak of the *p*-nitrophenolate ion at 400 nm decreased gradually with increasing time and almost disappeared after 3 min along with a concomitant increase of the peak at 300 nm of *p*-aminophenol.[24] In addition, GC-MS analysis showed that all the *p*-nitrophenol has been converted to *p*-aminophenol after the reaction (Figure S16). If an excess of $NaBH_4$ was used, pseudo-first-order kinetics could be used to evaluate the kinetic reaction rate of the current catalytic reaction.[26] As is shown in Figure 4c, a linear correlation of $\ln(C_t/C_0)$ versus reaction time is obtained (C_t and C_0 are *p*-nitrophenol concentrations at time t and 0, respectively). The kinetic constant k is calculated to be 0.815 min^{-1} (the uncertainty is 0.468%), which is not only much higher than previously reported cobalt-based catalysts such as cobalt nanoparticles in soft hydrogel (0.12 min^{-1})[27a] and cobalt microflowers (0.243 min^{-1})[27b] but also better than the noble metal catalysts such as Au (0.53 min^{-1}),[28] Ag (0.27 min^{-1}),[29] and Pd (0.732 min^{-1}).[30] A full comparison with cobalt and noble metal catalysts is shown in Table S1. From the comparison it can be seen that the Co@SiO_2 nanorattles have shown a larger kinetic constant with the least amount of $NaBH_4$, indicating a higher catalysis activity. The used catalysts were separated by a magnet and stored in air for 1 month; then the cycle test was carried out under the same conditions as for the first run. The lines of linear correlation are also shown in Figure 4c. The k decreases to 0.631 min^{-1} in the first cycle. In the following process, the reused catalyst also exhibits better catalytic activity than the Au and Ag catalysts,[28,29] and k is calculated to be 0.627, 0.623, and 0.565 min^{-1} in the next three cycles, respectively. Furthermore, the weight ratios of cobalt in Co@SiO_2 nanorattles were 9.25% (before catalysis) and 9.01% (after catalysis) on the basis of ICP measurement. Such a distinction might be attributed to the partial oxidation of cobalt nanoparticles during the storage time. The SEM (Figure S17) and HRTEM (Figure S18) images reveal that the morphology and structure of Co@SiO_2 nanorattles and the size of cobalt nanoparticles (20 nm) do not change significantly after four catalysis cycles. The IR spectra (Figure S19) of Co@SiO_2 nanorattles before and after catalysis do not differ either.

For investigating the effect of phase junctions in two-phase compositions, the catalytic capability of single-phase Co@SiO_2 nanorattles was also tested. Unlike the two-phase sample, the single-phase Co@SiO_2 nanorattles show a lower catalytic activity in the reduction of Nip under the same conditions.

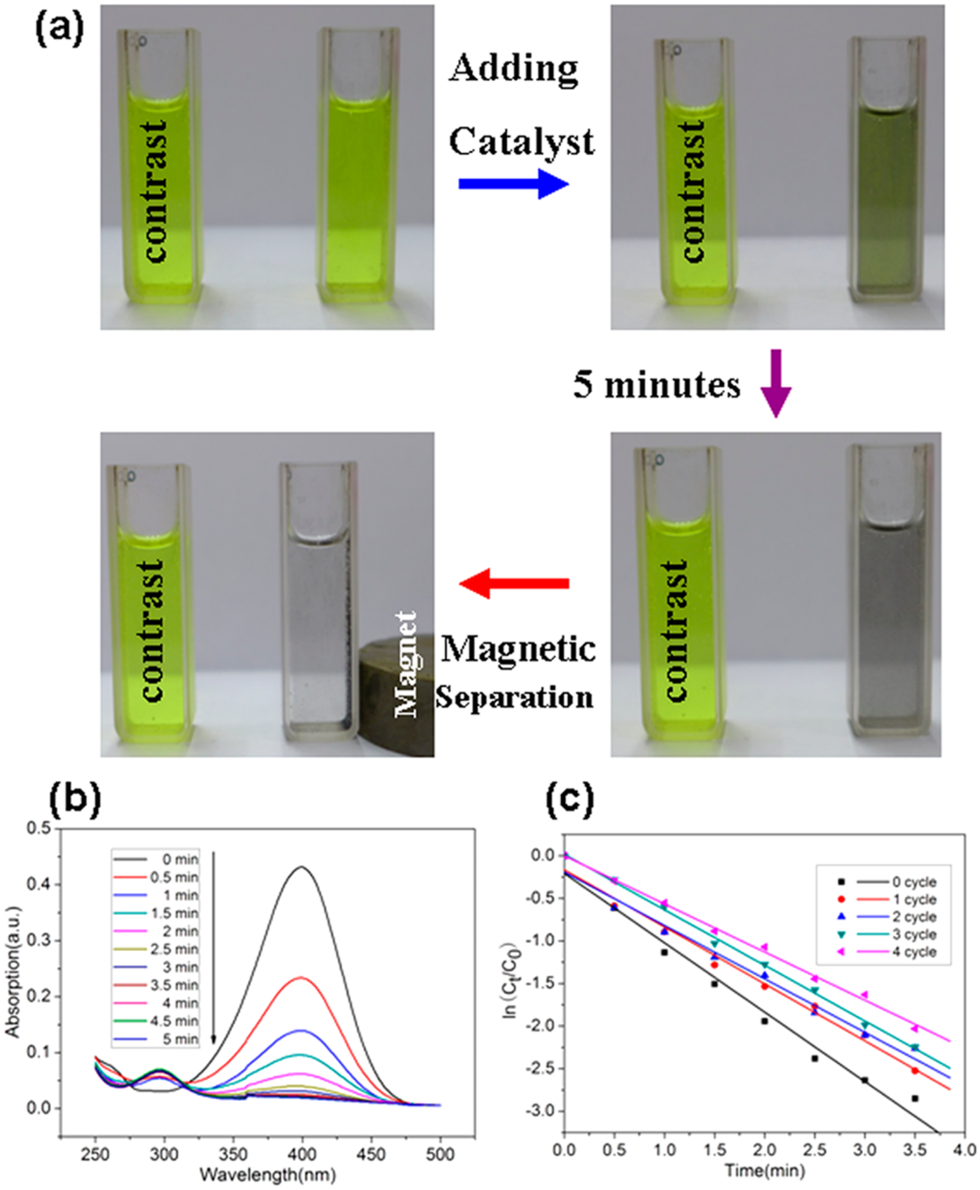

Figure 4. (a) Photographs of the catalysis process using Co@SiO_2 nanorattles as catalysts, (b) successive UV−vis spectra for the reduction reaction of *p*-nitrophenol by $NaBH_4$, and (c) kinetic curves for the reduction reaction of *p*-nitrophenol. C_t and C_0 are *p*-nitrophenol concentrations at time *t* and 0, respectively.

From the successive UV−vis spectra shown in Figure 5, the peak at 400 nm disappears after 16 min. The kinetic constants of the samples generated at 450 and 900 °C are calculated to be 0.105 and 0.143 min^{-1} according to the linear correlation shown in Figure 5, respectively, which is similar to the previous results reported for noble metal catalysts. In addition to the influence of specific area and pore size, such a phenomenon of decreasing activity may be attributed to the phase conversion. As for Co@SiO_2 nanorattles prepared at 600 °C, the fcc- and hcp-phase cobalt also constitute a phase junction, which is shown in Figure 3d. The Co 2p XPS spectra of different nanorattles are shown in Figure 6. The binding energy for Co $2p_{3/2}$ of the two-phase sample is 780.6 eV, which is lower than that of the single phases (hcp: 781.4 eV, fcc: 781.3 eV). This demonstrates a higher surface electron density of cobalt with a two-phase structure.[31] Considering that the reduction of Nip adsorbed on the surface by the surface-hydrogen species is the rate-determining step in the catalysis process,[24] the more surface electrons can enhance the electron transfer between the Nip molecules and cobalt nanoparticles owing to the different electronic structure of fcc- and hcp-phase cobalt,[19] thus increasing the catalytic activity of Co@ SiO_2 nanorattles. In order to study the influence of specific surface area and pore size on the catalytic activity, N_2 adsorption−desorption studies in the nanorattles annealed at 450 and 900 °C have been carried out. The N_2 absorption−desorption isotherms at 77 K and the pore size distribution of these two samples are shown in Figures S20 and S21, respectively. The specific surface area of the nanorattles annealed at 450 °C is 32.3 m^2 g^{-1}, and most pores are 20.1 nm in diameter, while the values of the nanorattles annealed at 900 °C are 11.9 m^2 g^{-1} and 22.3 nm, respectively. By comparing the three types of samples with different phases, it is found that the nanorattles with mixed phases (prepared at 600 °C) have an intermediate size of specific surface area and pores in the lowest nanometer range, which is enough for the reacting molecules to diffuse. Thus, it is

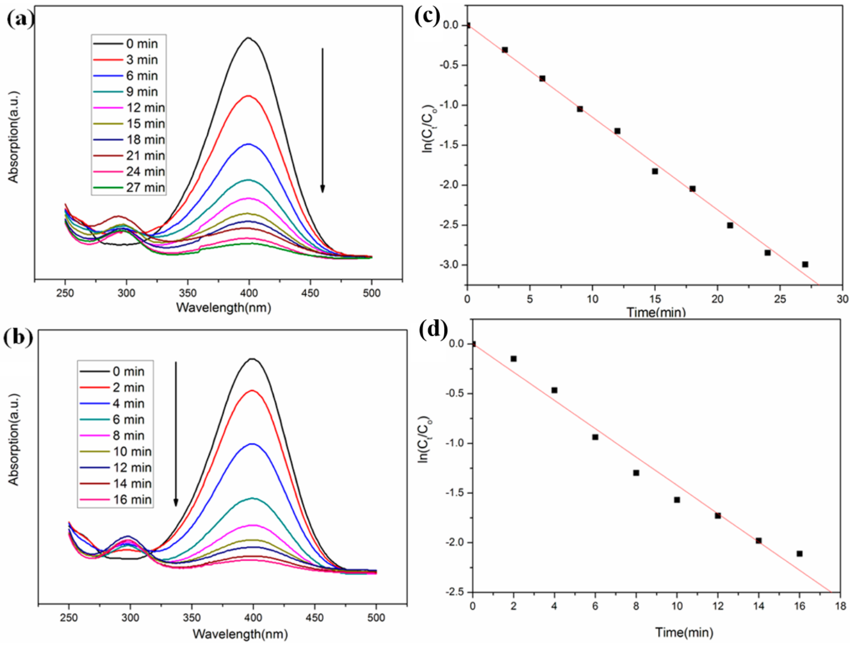

Figure 5. Successive UV−vis spectra for the reduction reaction of *p*-nitrophenol by $NaBH_4$ using the catalyst of $Co@SiO_2$ nanorattles: (a) hcp phase (450 °C), (b) fcc phase (900 °C). Kinetic curves for the reduction reaction of *p*-nitrophenol using the catalyst of $Co@SiO_2$ nanorattles: (c) hcp phase (450 °C), (d) fcc phase (900 °C). C_t and C_0 are *p*-nitrophenol concentrations at time *t* and 0, respectively.

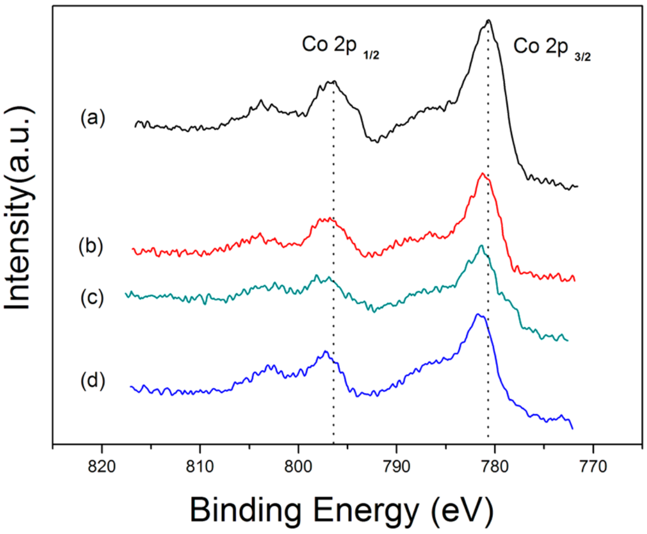

Figure 6. Co 2p XPS spectra of $Co@SiO_2$ nanorattles: (a) two-phase (600 °C), (b) hcp phase (450 °C), (c) fcc phase (900 °C), (d) two-phase after four catalysis cycles.

suggested that the change of specific surface area and pore size has no significant effect on the catalytic activity of the final product. The activity of a catalytic material can be exponentially improved as the catalyst is reduced in size at the nanoscale, which is attributed to an increase in the number of active sites. According to TEM images (Figure 3c, Figure S11, Figure S12), the average sizes of the Co nanoparticles generated at 450, 600, and 900 °C are about 18, 20, and 33 nm, respectively. Generally, the smaller the particle size, the higher the catalytic activity. However, the mixed-phase nanorattles in the middle nanometer range display higher catalytic activity than the other two types of single-phase products. It is, therefore, suggested that the mixture of phases plays a key role in the catalytic reduction. In addition, the binding energy for Co $2p_{3/2}$ after four catalysis cycles also shifts to a higher value of 781.6 eV, which indicates the oxidation of cobalt, corresponding to the weight ratio change of cobalt in $Co@SiO_2$ nanorattles.[32] This is the major cause of catalyst deactivation during the cycle test after storing in air for 1 month. Furthermore, the unique rattle-type structure, including porous shell and monodisperse cobalt cores, is effective for the reacting molecules in solution to diffuse into the interior of the nanorattles and increasing the active sites on cobalt cores for catalytic reaction. The pure Co nanoparticles generated at 600 °C also show a high catalytic activity. The kinetic constant *k* is calculated to be 0.379 min^{-1}, smaller than that of the nanorattles prepared at the same temperature (Figure S22). The decrease in catalytic activity can be attributed to the aggregation of Co nanopartcles, which leads to the decrease of surface active sites (Figure S23). Therefore, the single-phase $Co@SiO_2$ nanorattles also exhibit a high catalytic performance compared with noble metal nanocatalysts.

4. CONCLUSIONS

In summary, we have synthesized $Co@SiO_2$ nanorattles with hcp-Co and fcc-Co phase junctions as cores. The as-obtained nanorattles exhibited superior catalytic activity and stability during the heterogeneous catalytic reduction of *p*-nitrophenol, which is better than the previous cobalt and noble metal catalysts. The two-phase Co metal junctions displayed better performance than the single phase, suggesting the catalytic ability could be enhanced by making phase junctions in a single material. Moreover, it is confirmed that the unique rattle-type structure also helps to improve the catalytic ability of $Co@SiO_2$ nanoparticles. Considering the lower cost and higher catalyst activity, $Co@SiO_2$ nanorattles have the potential to be an alternative to noble metal catalysts.

■ ASSOCIATED CONTENT

Ⓢ Supporting Information

SEM and TEM images of the precursor, TGA-IR-MS curves, XRD patterns, SEM and TEM images of Co@SiO_2 nanorattles generated at 450 and 900 °C, and other data (BET, magnetism, GC-MS, IR) mentioned in the text (Figures S1−S23). A comparison of Co@SiO_2 nanorattles with other catalysts (Table S1). This material is available free of charge via the Internet at http://pubs.acs.org.

■ AUTHOR INFORMATION

Corresponding Author

*E-mail: cqw@ustc.edu.cn.

Notes

The authors declare no competing financial interest.

■ ACKNOWLEDGMENTS

This work was supported by the National Natural Science Foundation (NSFC, U1232211, 21271163) and Foundation of National Science Base (20772188).

■ REFERENCES

(1) (a) Murray, R. W. *Chem. Rev.* **2008**, *108*, 2688−2720. (b) Roucoux, A.; Schulz, J.; Patin, H. *Chem. Rev.* **2002**, *102*, 3757−3778.

(2) (a) Wang, D. S.; Li, Y. D. *Adv. Mater.* **2011**, *23*, 1044−1060. (b) Zhou, K. B.; Li, Y. D. *Angew. Chem., Int. Ed.* **2012**, *51*, 602−613.

(3) Tsung, C.-K.; Kuhn, J. N.; Huang, W.; Aliaga, C.; Hung, L.-I.; Somorjai, G. A.; Yang, P. *J. Am. Chem. Soc.* **2009**, *131*, 5816−5822.

(4) (a) Puntes, V. F.; Krishnan, K. M. A. P.; Alivisatos. *Science* **2001**, *291*, 2115−2117. (b) Santra, S.; Yang, H.; Holloway, P. H.; Stanley, J. T.; Mericle, R. A. *J. Am. Chem. Soc.* **2005**, *127*, 1656−1657. (c) Guczi, L.; Boskovic, G.; Kiss, E. *Catal. Rev.* **2010**, *52*, 133−203. (d) Wang, X.; Fu, H.; Peng, A.; Zhai, T.; Ma, Y.; Yao, J. *Adv. Mater.* **2009**, *21*, 1636−1640.

(5) (a) Khodakov, A. Y.; Chu, W.; Fongarland, P. *Chem. Rev.* **2007**, *107*, 1692−1744. (b) Qi, H.; Zhang, W.; Wang, X.; Li, H.; Chen, J.; Peng, K.; Shao, M. *Catal. Commun.* **2009**, *10*, 1178−1183.

(6) (a) Weststrate, C.; Hauman, M.; Moodley, D.; Saib, A.; van Steen, E.; Niemantsverdriet, C. J. *Top. Catal.* **2011**, *54*, 811−816. (b) Van Helden, P.; van den Berg, J.-A.; Westrate, C. J. *ACS Catal.* **2012**, *2*, 1097−1107. (c) Tyo, E. C.; Yin, C.; Vece, M.; Qian, Q.; Kwon, G.; Lee, S.; Lee, B.; DeBartolo, J. E.; Seifert, S.; Winans, R. E.; Si, R.; Ricks, B.; Goergen, S.; Rutter, M.; Zugic, B.; Flytzani-Stephanopoulos, M.; Wang, Z. W.; Palmer, R. E.; Neurock, M.; Vajda, S. *ACS Catal.* **2012**, *2*, 2409−2423. (d) Zhai, Y. P.; Pierre, D.; Si, R.; Deng, W. L.; Ferrin, P.; Nilekar, A. U.; Peng, G. W.; Herron, J. A.; Bell, D. C.; Saltsburg, H.; Mavrikakis, M.; Flytzani-Stephanopoulos, M. *Science* **2010**, *329*, 1633−1636. (e) Becker, M. J.; Xia, W.; Tessonnier, J. P.; Blume, R.; Yao, L. D.; Schlögl, R.; Muhler, M. *Carbon* **2011**, *49*, 5253−5264. (f) Zafeiratos, S.; Dintzer, T.; Teschner, D.; Blume, R.; Hävecker, M.; Knop-Gericke, A.; Schlögl, R. *J. Catal.* **2010**, *269*, 309−317.

(7) (a) Hashmi, A. S. K.; Hutchings, G. *Angew. Chem., Int. Ed.* **2006**, *45*, 7896−7936. (b) Hashmi, A. S. K.; Rudolph, M. *Chem. Soc. Rev.* **2008**, *37*, 1766−1775.

(8) Shylesh, S.; Schunemann, V.; Thiel, W. R. *Angew. Chem., Int. Ed.* **2010**, *49*, 3428−3459.

(9) Artero, V.; Chavarot-Kerlidou, M.; Fontecave, M. *Angew. Chem., Int. Ed.* **2011**, *50*, 7238−7266.

(10) Liu, J.; Qiao, S. Z.; Hu, Q. H.; Lu, G. Q. *Small* **2011**, *7*, 425−443.

(11) (a) Anand, C.; Srinivasu, P.; Mane, G. P.; Talapaneni, S. N.; Dhawale, D. S.; Wahab, M. A.; Priya, S. V.; Varghese, S.; Sugi, Y.; Vinu, A. *Microporous Mesoporous Mater.* **2013**, *167*, 146−154. (b) Zhang, X.; Wei, Z.; Guo, Q.; Tian, H. *J. Power Sources* **2013**, *231*, 190−196.

(12) (a) Zhang, J.; Xu, Q.; Feng, Z. C.; Li, M. J.; Li, C. *Angew. Chem., Int. Ed.* **2008**, *47*, 1766−1769. (b) Wang, X.; Xu, Q.; Li, M. R.; Shen, S.; Wang, X. L.; Wang, Y. C.; Feng, Z. C.; Shi, J. Y.; Han, H. X.; Li, C. *Angew. Chem., Int. Ed.* **2012**, *51*, 13089−13092. (c) Tsukamoto, D.; Shiraishi, Y.; Sugano, Y.; Ichikawa, S.; Tanaka, S.; Hirai, T. *J. Am. Chem. Soc.* **2012**, *134*, 6309−6315.

(13) de la Peña O'Shea, V. A.; de P. R. Moreira, I.; Roldán, A.; Illas, F. *J. Chem. Phys.* **2010**, *133*, 024701−024708.

(14) Liu, J.; Qiao, S. Z.; Chen, J. S.; Lou, X. W.; Xing, X.; Lu, G. Q. *Chem. Commun.* **2011**, *47*, 12578−12591.

(15) Chen, Z.; Cui, Z.-M.; Niu, F.; Jiang, L.; Song, W.-G. *Chem. Commun.* **2010**, *46*, 6524−6526.

(16) (a) Chen, Y.; Chen, H.; Guo, L.; He, Q.; Chen, F.; Zhou, J.; Feng, J.; Shi, J. *ACS Nano* **2010**, *4*, 529−539. (b) Zhu, Y.; Ikoma, T.; Hanagata, N.; Kaskel, S. *Small* **2010**, *6*, 471−478. (c) Lee, J.; Park, J. C.; Bang, J. U.; Song, H. *Chem. Mater.* **2008**, *20*, 5839−5844. (d) Fang, Z.; Liu, Y. F.; Liu, X. W.; Wang, Q.; Fan, Y. T.; Wang, W. Z. *CrystEngComm* **2011**, *13*, 5653−5657.

(17) Yan, N.; Chen, Q. W.; Wang, F.; Wang, Y.; Zhong, H.; Hu, L. *J. Mater. Chem. A* **2013**, *1*, 637−643.

(18) Yan, N.; Hu, L.; Li, Y.; Wang, Y.; Zhong, H.; Hu, X. Y.; Kong, X. K.; Chen, Q. W. *J. Phys. Chem. C* **2012**, *116*, 7227−7235.

(19) Srivastava, A. K.; Madhavi, S.; White, T. J.; Ramanujan, R. V. *J. Mater. Chem.* **2005**, *15*, 4424−4428.

(20) Dinega, D. P.; Bawendi, M. G. *Angew. Chem., Int. Ed.* **1999**, *38*, 1788−1791.

(21) (a) Liu, Q. Y.; Guo, X. H.; Li, Y.; Shen, W. J. *Langmuir* **2009**, *25*, 6425−6430. (b) Zhang, Y.; Yao, Q.; Zhang, Y.; Cui, T.; Li, D.; Liu, W.; Zhang, Z. *Cryst. Growth Des.* **2008**, *8*, 3206−3212.

(22) Yan, N.; Wang, F.; Zhong, H.; Li, Y.; Wang, Y.; Hu, L.; Chen, Q. W. *Sci. Rep.* **2013**, *3*, 1568.

(23) Bennetta, H. L.; Torre, D. E. *J. Appl. Phys.* **2005**, *97*, 10E502, 1−3.

(24) Hervés, P.; Pérez-Lorenzo, M.; Liz-Marzán, L. M.; Dzubiella, J.; Lu, Y.; Ballauff, M. *Chem. Soc. Rev.* **2012**, *41*, 5577−5587.

(25) Du, D. Y.; Qin, J. S.; Wang, T. T.; Li, S. L.; Su, Z. M.; Shao, K. Z.; Lan, Y. Q.; Wang, X. L.; Wang, E. B. *Chem. Sci.* **2012**, *3*, 705−710.

(26) (a) Wunder, S.; Polzer, F.; Lu, Y.; Mei, Y.; Ballauff, M. *J. Phys. Chem. C* **2010**, *114*, 8814−8820. (b) Wunder, S.; Lu, Y.; Albrecht, M.; Ballauff, M. *ACS Catal.* **2011**, *1*, 908−916.

(27) (a) Sahiner, N.; Ozay, H.; Ozay, O.; Aktas, N. *Appl. Catal., B* **2010**, *101*, 137−143. (b) Senapati1, S.; Srivastava1, S. K.; Singh, S. B. *J. Nanosci. Nanotechnol.* **2012**, *12*, 3048−3058.

(28) Deng, Y.; Cai, Y.; Sun, Z.; Liu, J.; Liu, C.; Wei, J.; Li, W.; Liu, C.; Wang, Y.; Zhao, D. *J. Am. Chem. Soc.* **2010**, *132*, 8466−8473.

(29) Ai, L. H.; Yue, H. T.; Jiang, J. *J. Mater. Chem.* **2012**, *22*, 23447−23453.

(30) Lu, X.; Bian, X.; Nie, G.; Zhang, C.; Wang, C.; Wei, Y. *J. Mater. Chem.* **2012**, *22*, 12723−12730.

(31) Gao, M. R.; Xu, Y. F.; Jiang, J.; Zheng, Y. R.; Yu, S. H. *J. Am. Chem. Soc.* **2012**, *134*, 2930−2933.

(32) Yang, H. T.; Su, Y. K.; Shen, C. M.; Yang, T. Z.; Gao, H. J. *Surf. Interface Anal.* **2004**, *36*, 155−160.